shear wave attenuation, and it has been inferred that a crustal magma chamber is present beneath this area (*22*), but this has not yet been confirmed. Our radar interferometry observations of deformation in southwest Iceland show that the technique can be used to monitor long-term strain buildup at plate boundaries and volcanoes and therefore may help to increase understanding of the preparatory processes of earthquakes and eruptions.

REFERENCES AND NOTES

1. In 1938, the first crustal deformation geodetic network was installed in Iceland, designed to detect extension across the North Iceland rift zone [O. Niemczyk, *Spalten auf Island* (Wittwer, Stuttgart, Germany, 1943)].
2. E. Tryggvason, *Cont. Oceanic Rifts Geodyn. Ser.* **8**, 17 (1982).
3. See, for example, G. R. Foulger *et al.*, *Nature* **358**, 488 (1992); F. Sigmundsson, P. Einarsson, R. Bilham, E. Sturkell, *J. Geophys. Res.* **100**, 6235 (1995).
4. According to the NUVEL-1A global plate motion model by C. DeMets, R. G. Gordon, D. F. Argus, and S. Stein [*Geophys. Res. Lett.* **21**, 2191 (1994)].
5. K. Saemundsson and S. Einarsson, *Geological Map of Iceland, Sheet 3, SW-Iceland, 2nd ed.* (Icelandic Museum of Natural History and Icelandic Geodetic Survey, Reykjavik, Iceland, 1980); P. Einarsson and K. Saemundsson, accompanying map in *I Hlutarins Edli*, T. Sigfusson, Ed. (Menningarsjodur, Reykjavik, Iceland, 1987).
6. P. Einarsson, *Tectonophysics* **189**, 261 (1991); F. W. Klein, P. Einarsson, M. Wyss, *J. Geophys. Res.* **78**, 5084 (1973); *ibid.* **82**, 865 (1977); P. Halldorsson, R. Stefansson, P. Einarsson, S. Bjornsson, *Estimate of Earthquake Risk* (Ministry of Industry, Reykjavik, Iceland, 1984).
7. R. G. Gordon and S. Stein, *Science* **256**, 333 (1992).
8. M. Lisowski, J. C. Savage, W. H. Prescott, *J. Geophys. Res.* **96**, 8369 (1991).
9. E. Sturkell, F. Sigmundsson, P. Einarsson, R. Bilham, *Geophys. Res. Lett.* **21**, 125 (1994).
10. H. Eysteinsson, *Leveling and Gravity Measurements in the Outer Part of the Reykjanes Peninsula 1992* (Report OS-93029, National Energy Authority, Reykjavik, Iceland, 1993).
11. E. Tryggvason, in *Geodynamics of Iceland and the North Atlantic Area*, L. Kristjánsson, Ed. (Reidel, Dordrecht, Netherlands, 1974), pp. 241–262; E. Tryggvason, *Vertical Component of Ground Deformation in Southwest and North Iceland* (Report 8102, Nordic Volcanological Institute, Reykjavik, Iceland, 1981).
12. D. Massonnet *et al.*, *Nature* **364**, 138 (1993); D. Massonnet, K. Feigl, M. Rossi, F. Adragna, *ibid.* **369**, 227 (1994); D. Massonnet, W. Thatcher, H. Vadon, *ibid.* **382**, 612 (1996); D. Massonnet, P. Briole, A. Arnaud, *ibid.* **375**, 567 (1995); R. M. Goldstein, H. Engelhardt, B. Kamb, R. M. Frolich, *Science* **262**, 1525 (1993).
13. The ERS-1 and ERS-2 satellites have sun-synchronous near polar orbits, with a mean altitude of 785 km and an inclination of 98.5°. The orbital cycle is 35 days in normal operational phase. Onboard SAR instruments operate in the C band, with a wavelength of 5.656 cm.
14. D. Massonnet and K. Feigl, *Geophys. Res. Lett.* **22**, 1537 (1995).
15. D. Massonnet, H. Vadon, M. Rossi, *IEEE Trans. Geosci. Remote Sens.* **34**, 489 (1996).
16. The coherence of an interferogram measures the similarity of a pixel phase to the phase of its neighbors. When fringes in an interferogram can be visually discriminated, its coherence is good. Change in surface characteristics reduces coherence. When the same radar image exhibits low coherence whatever the image it is paired with, it generally means "climatic damage" to the radar image (such as that caused by snow cover).
17. M. A. Grant, I. G. Donaldson, P. F. Bixley, *Geothermal Reservoir Engineering* (Academic Press, New York, 1982).
18. The Mogi model was first applied to active volcanoes by K. Mogi [*Bull. Earthquake Res. Inst. Univ. Tokyo* **36**, 99 (1958)]. It was originally derived for a point source of pressure in an elastic half-space, but D. F. McTigue [*J. Geophys. Res.* **92**, 12931 (1987)] showed that it performs well for spherical sources of finite size, as long as $(a/d_{mogi})^5 \ll 1$, where a is the source radius. Surface subsidence is expressed as $h_{mogi}\, d_{mogi}^{3} (d_{mogi}^{2} + r^{2})^{-3/2}$, where r is the horizontal distance from the source. Horizontal radial displacement is $h_{mogi}\, d_{mogi}^{2}\, r\, (d_{mogi}^{2} + r^{2})^{-3/2}$.
19. If $v_{spreading}$ is parallel to the plate boundary, then Eq. 1 reduces to a model frequently used for strain accumulation across strike-slip faults [see, for example, J. C. Savage and R. O. Burford *J. Geophys. Res.* **78**, 832 (1973) and (*8*)].
20. We consider the source to represent the effect of material loss beneath d_{lock} because ductile extension there is not balanced by inflow of material from below. Surface subsidence caused by a line-source of pressure within an elastic half-space can be obtained by integration of the Mogi model (*18*). The model was first applied to Iceland rifts by E. Tryggvason [*J. Geophys. Res.* **73**, 7039 (1968)].
21. G. Bjornsson and B. Steingrimsson, *Temperature and Pressure in the Svartsengi Geothermal System* (Report 91016, National Energy Authority, Reykjavik, Iceland, 1991).
22. B. Brandsdottir, P. Einarsson, K. Arnason, H. Kristmannsdottir, *Refraction Measurements and Seismic Monitoring During an Injection Experiment at the Startsengi Geothermal Field in 1993* (Report RH-03-94, Science Institute, University of Iceland, Reykjavik, Iceland, 1994).

23. We thank two anonymous reviewers for comments, D. Massonnet for discussion and an early review of the manuscript, K. Feigl for discussion, and the European Commission for financial support for F.S. (grant PL95027). The General Mapping Tool public domain software was used to prepare figures.

16 August 1996; accepted 13 November 1996

Recalibrated Mariner 10 Color Mosaics: Implications for Mercurian Volcanism

Mark S. Robinson* and Paul G. Lucey

Recalibration of Mariner 10 color image data allows the identification of distinct color units on the mercurian surface. We analyze these data in terms of opaque mineral abundance, iron content, and soil maturity and find color units consistent with the presence of volcanic deposits on Mercury's surface. Additionally, materials associated with some impact craters have been excavated from a layer interpreted to be deficient in opaque minerals within the crust, possibly analogous to the lunar anorthosite crust. These observations suggest that Mercury has undergone complex differentiation like the other terrestrial planets and the Earth's moon.

One unresolved question from the Mariner 10 exploration of Mercury is whether widespread plains deposits formed due to volcanism or basin formation–related impact ejecta (*1–3*). We recalibrated and analyzed the Mariner 10 first encounter approach color data to address this fundamental issue. Previous analyses of Mariner 10 images defined color units on Mercury which indicated that color boundaries often did not correspond to photogeologic units, and no low albedo relatively blue mercurian materials were found that correspond to lunar mare deposits (*4, 5*). The calibration employed in these earlier studies did not completely remove vidicon blemishes and radiometric residuals. These artifacts were sufficiently severe that the authors presented an interpretive color unit map overlaid on monochromatic mosaics while publishing only a subset of the color ratio coverage of Mercury (*4–7*). We derived a refined calibration that increased the signal-to-noise ratio of these mercurian image data. These recalibrated image mosaics show the complete ultraviolet (UV) orange color data for this portion of Mercury. We interpret these recalibrated data in terms of the current paradigm of visible color reflectance for iron-bearing silicate regoliths (*5, 6, 8*).

The Mariner 10 vidicon imaging system was spatially nonuniform in bias and dark current, as well as being nonlinear at the extremes of the light transfer curve (*9*). Prelaunch flat field images acquired at varying exposure times allowed for the derivation of a nonlinearity and sensitivity nonuniformity correction, while an average of inflight images of deep space corrected for system offset (*10*). We utilized low-contrast Mariner 10 images of the venusian atmosphere to identify vidicon blemishes and create a stencil from which affected areas were simply deleted from all the mercurian images. Two spatially redundant mercurian mosaic sequences were processed for each filter and thus little areal coverage was lost due to the blemish deletion procedure. Instead of overlaying each image during the mosaicking, the images were averaged so that each pixel was formed from one to seven frames. The data were resampled to 3 km per pixel (original data were 2 to 3 km per pixel)

M. S. Robinson, United States Geological Survey, 2255 North Gemini Drive, Flagstaff, Arizona, 86001, USA.
P. G. Lucey, Hawaii Institute of Geophysics and Planetology, University of Hawaii, Honolulu, HI 96822, USA.

*To whom correspondence should be addressed. E-mail: robinson@flagmail.wr.usgs.gov

centered at the subspacecraft point to enhance the signal-to-noise ratio of the mosaics. The averaging technique, conservative resampling, and blemish deletion reduced the effects of system noise, bit errors, and calibration residuals such that subtle color units can be identified. Absolute calibration was derived by photometrically normalizing the images to 0° phase, using the equations of Hapke (*11*), and deriving a coefficient such that the disc-integrated average of the orange mosaic (575 nm) matches the Earth-based telescopic, disc-integrated 554-nm geometric albedo of 0.14 (*12*). The disc-integrated value from the photometrically normalized UV (355 nm) mosaic was adjusted to match a value 0.6 that of the orange value, which corresponds to the mercurian spectral slope derived from Earth-based measurements (*13*).

Terrestrial-based remote sensing studies (*14–16*) and photogeology (*3*) indicate that Mercury has a silicate crust bearing minerals such as feldspars, pyroxenes, and olivine (*4–6*). Rava and Hapke (*5*) provided an interpretive framework to understand the spectral properties of Mercury, based on the assumption of a lunar-like surface composition. In general, the addition of ferrous iron to a silicate mineral or glass darkens the material and reddens the visible spectral slope [decreases the UV/orange color ratio (*17, 18*); see Fig. 1]. This correlation of albedo and color ratio due to variations in ferrous iron is mimicked by variation of maturity of lunar, and likely mercurian, soils. In the course of the space-weathering maturation process, vacuum reduction of ferrous iron to submicroscopic native iron causes relatively blue immature soils to darken and spectrally redden (*19*). Thus, since the Mariner 10 data examined here consist of only two wavelengths, it is problematic to decouple the spectral effects of ferrous iron content and maturity due to space weathering. However, increases in the abundance of spectrally neutral opaque minerals, such as ilmenite, tend to darken but decrease the spectral redness of silicate soils (*5, 20*) (Fig. 1). Rotation of two key parameters (UV/orange ratio versus orange albedo), so that the two trends are perpendicular to the axes, should result in decoupling the effects of ferrous iron plus maturity and opaque mineral abundance variations. This coordinate rotation results in images of two parameters (Fig. 2), one sensitive to ferrous iron plus maturity and the other to opaque mineral content (*18*). It is apparent that spatially coherent structures in the parameter 1 image (iron plus maturity, Fig. 2C) are mostly associated with crater rays and ejecta, suggesting that this parameter is dominated by maturity variations. The spatial patterns in the parameter 2 image (opaque content, Fig. 2D) are not re-

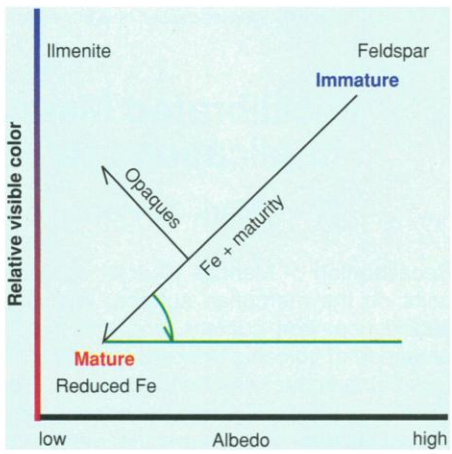

Fig. 1. The visible color of the lunar surface (and Mercury by inference) can be described by two perpendicular trends (opaque mineral concentration and iron plus maturity). The addition of ferrous iron to a silicate material tends to redden the visible slope and lower the albedo (a translation down the iron-maturity line). Paralleling the iron trend, immature soils are bluer and have higher albedo (orange brightness) than mature soils; as soils mature their reflectance would also translate down the iron-maturity line. The addition of spectrally neutral opaque minerals, such as ilmenite, results in a trend that is nearly perpendicular to the iron-maturity line: opaques darken and increase the relative color ratio (UV brightness/orange brightness) of silicate soils. Materials that compose much of the lunar surface and dominantly control these trends (discussed in text) are plotted in their relative positions. These two trends can be used to map the distribution of opaques (opaque index) and the iron-maturity parameter through a coordinate rotation (indicated by the green curve) such that their perpendicular axes become parallel with the *x* and *y* axes of the color-albedo plot (*18*).

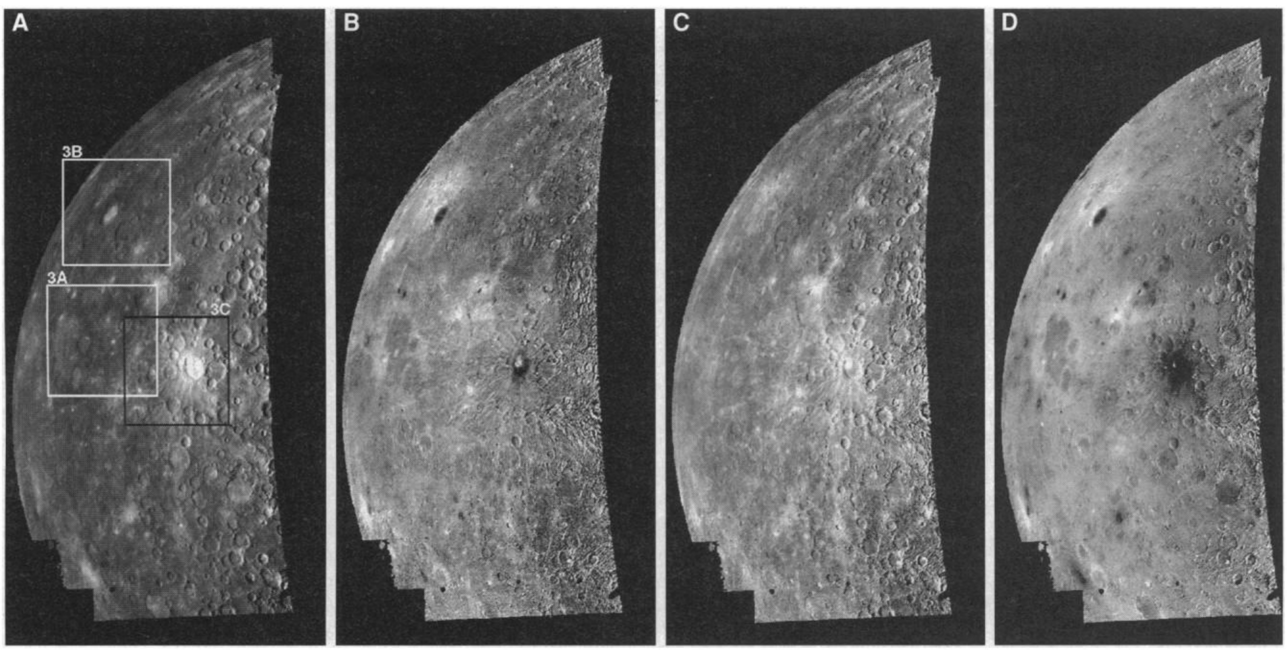

Fig. 2. Essential spectral parameters for the mercurian data examined here. (**A**) Orange (575 nm) albedo (*25*); lettered boxes indicate areas enlarged in Fig. 3; (**B**) relative color (UV/orange); brighter tones indicate increasing blueness; (**C**) parameter 1, iron-maturity parameter; brighter tones indicate decreasing maturity and iron content; and (**D**) parameter 2, opaque index; brighter tones indicate increasing opaque mineral content. The relatively bright feature in the center right of the albedo image is the Kuiper-Muraski crater complex centered at latitude 12°S, longitude 31°E. A qualitative assessment of the calibration residual is the lack of frame boundaries visible in the ratio image.

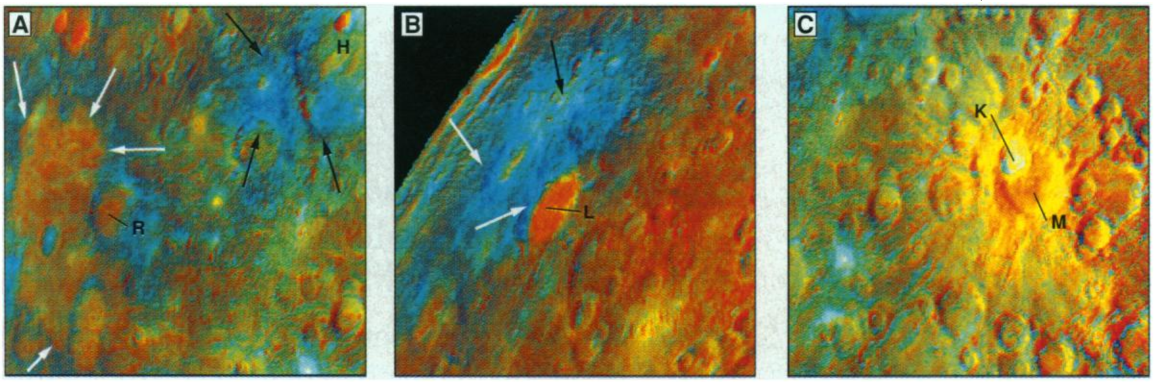

Fig. 3. Enhanced color composite enlargements showing geologic relationships discussed in the text for areas labeled by boxes in Fig. 2. Red is formed as inverse of the opaque index (increasing redness indicates decreasing opaque mineralogy; Fig. 2D); green component is the iron-maturity parameter (Fig. 2C); and blue shows the relative color (UV/orange ratio; Fig. 2B). (**A**) The plains unit seen west and south, and filling the interior of the crater Rudaki (labelled R, with a crater diameter of 120 km) exhibits embaying boundaries (white arrows) indicative of a material emplaced as a flow and has a distinct color signature relative to its surroundings. The blue material on the southwest margin of the crater Homer (H, 320 km diameter) exhibits diffuse boundaries, is insensitive to local topographic undulations (black arrows), and is aligned along a linear segment of a Homer basin ring. (**B**) A portion of the blue material seen northwest of crater Lermontov (L, 160 km diameter) is somewhat concentric to a small impact crater (black arrow) and may represent material excavated from below during the impact. However, examination of the iron-maturity parameter and opaque index images (Fig. 2) suggest that the darkest and bluest material (white arrows) in this deposit is not associated with an impact ejecta pattern; rather, the anomalous lighter blue ejecta is composed of the darker material, though less mature and possibly with an admixture of basement material, overlying the darker blue portions of the deposit. (**C**). The Kuiper-Muraski crater complex (K and M, respectively) materials have a very low opaque content (Fig. 2D), while Kuiper (60 km diameter) is brighter and bluer than Muraski (125 km diameter; Fig. 2, A and B), however, this difference is most likely maturity (Fig. 2C).

lated to ejecta or crater rays and so are most likely compositional units formed by other geologic processes.

Widespread plains deposits have been identified on Mercury and it is controversial whether these deposits are related to large impact basin formation or volcanism (*1–3*). Impact-related origins have been proposed for the mercurian plains because they do not show high-contrast albedo boundaries with the surroundings, analogous to impact-related light plains on the moon, such as the Cayley formation, which appear to be largely remobilized local material (*2*, *3*). However, volcanic plains deposits do occur on the moon, such as the Apennine Bench formation (*21*, *22*), with distinct composition and do not exhibit high-contrast albedo boundaries; thus, albedo is not a definitive diagnostic indicator of composition or compositional differences. Nevertheless, compositional contrast (detectable by color differences) with surrounding material remains a key indicator of volcanic versus basin-related origin for a plains deposit.

Our recalibration has reduced the systematic noise in the Mariner 10 data set such that correlations between morphologic and color boundaries can be discerned. A plains unit west of Rudaki crater is defined by embayment relations of distinct color boundaries (Fig. 3) that correspond to previously mapped plains boundaries (*23*). The Rudaki plains have an intermediate opaque index and overlies darker materials that have higher opaque indices. These spectral relationships suggest that the Rudaki-type plains are compositionally distinct from their surroundings and demonstrate that at least some of the extensive plains units on Mercury were emplaced as volcanic flows (Fig. 3).

The Rudaki plains (and similar plains seen in Fig. 2) do not appear as anomalies in the ferrous iron plus maturity image (Fig. 2C), indicating that they have similar FeO contents to the rest of the mercurian crust in this image. The mercurian global crustal abundance of FeO has been estimated to be less than 6% by weight (*13–15*). Sprague *et al.* (*15*) tentatively identified a basalt-like material in this hemisphere with Earth-based thermal infrared measurements, while later microwave measurements indicated a paucity of areally significant basaltic materials on Mercury (*16*). From the Mariner 10 data presented here, we cannot make a definitive identification of a low iron basaltic material; however, the spectral parameters, stratigraphic relations, and morphology are consistent with such a material.

Volcanic materials can be ballistically emplaced as pyroclastic deposits. Figure 3A shows dark blue material exhibiting diffuse boundaries consistent with ballistically emplaced material. There is no impact crater central to these deposits and they straddle a linear segment of a ring of Homer basin that could serve as a weakness in the crust, allowing magma to reach the surface, morphology consistent with a pyroclastic origin as explosive fissure eruptions. A similar spectral unit occurs northwest of the crater Lermontov (Fig. 3B); both exhibit relatively blue color, high opaque index, and low albedo, which is consistent with a more mafic material. If these units are pyroclastic in origin, they represent not only a distinct composition, but an important clue to the volatile history of the planet.

One of the most striking features shown in Figs. 2 and 3 is the Kuiper-Muraski crater complex. Kuiper, superposed on the crater Muraski (Fig. 3B), is one of the youngest large impact craters on Mercury (*3*). Kuiper has an opaque index equivalent to Muraski, but the iron-maturity parameter indicates that Kuiper is relatively immature, consistent with its fresher morphology, thus explaining the color difference (relatively blue). The opaque index for both materials is very low, possibly similar to a lunar soil formed from an anorthositic crust. For the portions of Mercury shown in Fig. 2, the regions with the lowest opaque index are associated with craters, consistent with excavation of a layer at depth that is deficient in opaque minerals (Fig. 2D) resurfaced by later processes. This layer may be analogous to an ancient lunar anorthosite crust. Consistent with this hypothesis, Earth-based remote sensing has tentatively identified anorthosite on Mercury (*15*).

The distinct color units identified here suggest that the mercurian crust is compositionally heterogeneous and poorly mixed on the scale of the Mariner 10 data (3 km). Additionally, the suggestion of areally significant volcanic materials on Mercury implies that volcanism may have played a significant role in global cooling and thus, thermal models of the planet might be reexamined (*16*, *24*).

REFERENCES AND NOTES

1. B. C. Murray, *J. Geophys. Res.* **80**, 2342 (1975); B. C. Murray *et al.*, *Science* **185**, 169 (1974); R. G. Strom, *Phys. Earth Planet. Inter.* **15**, 156 (1977); D. Dzurisin, *J. Geophys. Res.* **83**, 4883 (1978); W. S. Keiffer and B. C. Murray, *Icarus* **72**, 477 (1987).
2. D. E. Wilhelms, *Icarus* **28**, 551 (1976).
3. P. D. Spudis and J. E. Guest, in *Mercury*, F. Vilas, C. R. Chapman, M. S. Matthews, Eds. (Univ. of

Arizona Press, Tucson, AZ, 1988), pp. 118–164.
4. B. Hapke, C. Christman, B. Rava, J. Mosher, *Proc. Lunar Planet. Sci. Conf.* **11**, 817 (1980).
5. B. Rava and B. Hapke, *Icarus* **71**, 397 (1987).
6. B. Hapke, G. E. Danielson, K. Klaasen, L. Wilson, *J. Geophys. Res.* **80**, 2431 (1975).
7. B. Hapke, *J. Atmos. Sci.* **33**, 1803 (1976).
8. M. J. Cintala, *J. Geophys. Res.* **97**, 947 (1992).
9. M. Benesh and M. Morrill, *Jet Propul. Lab. Doc. 615-148* (1973); G. E. Danielson, K. P. Klaasen, J. L. Anderson, *J. Geophys. Res.* **80**, 2357 (1975); J. M. Soha *et al.*, *ibid.*, p. 2394.
10. M. S. Robinson, B. R. Hawke, P. G. Lucey, *J. Geophys. Res.* **97**, 18265 (1992). The offset (signal inherent in the imaging system when no photons are impinging on the detector) was derived by averaging images acquired during the color sequence where Mercury did not appear in the frame—the camera was imaging nothing but deep space. As a test of the stability of the offset during the imaging sequence, the average offset image was subtracted from each frame of space acquired during the color sequence and no significant drift was measurable (camera A average residual was 0.3 DN; camera B average residual was 0.1 DN; possible range of DN 0–255). Examination of overlap between calibrated frames (dark corrected and linearized) revealed a maximum mismatch of 5%, with the average being 2%. Averaging areas of overlap between multiple frames reduced this residual in the final mosaics.
11. Applying Hapke modeling [B. W. Hapke, *Icarus* **67**, 264 (1986)] with parameters derived for the moon [P. Helfenstein and J. Veverka, *ibid.* **72**, 343 (1987); (*12*)] and those derived for Mercury resulted in overcorrection at the mercurian poles. Previous work with Galileo solid-state imager data has shown that Θ (theta bar) can be adjusted to compensate for such an overcorrection [A. S. McEwen and T. L. Becker, *Lunar Planet. Sci.* **XXIV**, 955 (1993)]. Iterative adjustment and visual inspection of the photometric flatness of the mercurian mosaic led us to use the following values for the Hapke parameters: $w = 0.21$, $h = 0.07$, $B_0 = 2.0$, $b = 0.29$, $c = 0.39$, and Θ (theta bar) = 15. It is known that the lunar photometric function varies subtly as a function of wavelength and composition (see McEwen and Becker, above), and the same is most likely true for Mercury. However, such minor effects will not hinder our identification of relative local color boundaries, which are key to the science presented here.
12. B. Hapke, *Phys. Earth Planet. Inter.* **15**, 264 (1977); J. Veverka, P. Helfenstein, B. Hapke, J. D. Goguen, in *Mercury*, F. Vilas, C. Chapman, M. S. Mathews, Eds. (Univ. of Arizona Press, Tucson, 1988) pp. 37–58.
13. F. Vilas, in *Mercury*, F. Vilas, C. Chapman, M. S. Mathews Eds. (Univ. of Arizona Press, Tucson, 1988) pp. 59–76.
14. T. B. McCord and J. B. Adams, *Icarus* **17**, 585 (1972); F. Vilas and T. B. McCord, *ibid.* **28**, 593 (1976); F. Vilas, M. A. Leake, W. W. Mendell, *ibid.* **59**, 60 (1984); F. Vilas, *ibid.* **64**, 133 (1985).
15. A. L. Sprague, R. W. H. Kozlowski, F. C. Witteborn, D. P. Cruikshank, D. H. Wooden, *ibid.* **109**, 156 (1994).
16. R. Jeanloz, D. L. Mitchell, A. L. Sprague, I. de Pater, *Science* **268**, 1455 (1995).
17. J. B. Adams, *J. Geophys. Res.* **79**, 4829 (1974).
18. P. G. Lucey, D. T. Blewett, J. L. Johnson, G. J. Taylor, B. R. Hawke, *Lunar Planet. Sci.* **XXVII**, 781 (1996).
19. B. Hapke, W. Cassidy, E. Wells, *Moon* **13**, 339 (1975); B. Hapke, in (*12*); R. V. Morris, *Proc. Lunar Planet. Sci. Conf.* **11**, 1697 (1980).
20. M. P. Charette, T. B. McCord, C. Pieters, J. B. Adams, *J. Geophys. Res.* **79**, 1605 (1974); E. Wells and B. Hapke, *Science* **195**, 977 (1977).
21. P. D. Spudis, *Proc. Lunar Planet. Sci. Conf.* **9**, 3379 (1978).
22. B. R. Hawke and J. W. Head, *ibid.*, p. 3285.
23. R. A. DeHon, D. H. Scott, J. R. Underwood, *U.S. Geol. Surv. Misc. Invest. Series Map I-1233* (1981).
24. T. Spohn, *Icarus* **90**, 222 (1991).
25. We find that the highest albedo materials in the mosaic (that is, crater Kuiper) are only about two times the global average (0.29 versus 0.14, respectively), whereas Hapke *et al.* (6) report the floor of Kuiper to be about three times the global average (0.45 versus 0.14). We are unable to explain the discrepancy satisfactorily and assume that it is due to improvements in our calibration.
26. We thank B. Hapke, G. J. Taylor, and B. R. Hawke for helpful reviews.

13 September 1996; accepted 6 December 1996

Activation of SAPK/JNK by TNF Receptor 1 Through a Noncytotoxic TRAF2-Dependent Pathway

Gioacchino Natoli,* Antonio Costanzo, Angelo Ianni, Dennis J. Templeton, James R. Woodgett, Clara Balsano, Massimo Levrero

Interaction of the p55 tumor necrosis factor receptor 1 (TNF-R1)–associated signal transducer TRADD with FADD signals apoptosis, whereas the TNF receptor–associated factor 2 protein (TRAF2) is required for activation of the nuclear transcription factor nuclear factor kappa B. TNF-induced activation of the stress-activated protein kinase (SAPK) was shown to occur through a noncytotoxic TRAF2-dependent pathway. TRAF2 was both sufficient and necessary for activation of SAPK by TNF-R1; conversely, expression of a dominant-negative FADD mutant, which blocks apoptosis, did not interfere with SAPK activation. Therefore, SAPK activation occurs through a pathway that is not required for TNF-R1–induced apoptosis.

Tumor necrosis factor is a pleiotropic cytokine that has growth modulatory, cytotoxic, and inflammatory activities (*1*). The effects of TNF are mediated by two distinct cell surface receptors of about 55 kD (TNF-R1) and 75 kD (TNF-R2), which are expressed on almost all nucleated cells (*2*). Proteins that are recruited to TNF-Rs after activation have been molecularly cloned, and their function has been partially characterized (*3*). The TNF-R1–associated death domain (TRADD) protein interacts with TNF-R1 upon TNF-induced trimerization, and its overexpression is sufficient to cause both activation of NFκB and apoptosis (*4, 5*). Other proteins associated with TNF-R1 by way of TRADD include the death domain protein FADD (*5, 6*) (which also participates in the transduction of Fas-induced apoptotic signals) and TRAF2 (*5, 7*). TRAF2 belongs to a family of signal transducers for both the TNF-R superfamily and interleukin-1 receptor I (*8*). The TRAF family is characterized by a conserved COOH-terminal TRAF domain and, with the exception of TRAF1, an NH_2-terminal RING finger, which is relevant for signal transduction (*8, 9*). An additional molecule required for TNF-R1 signal transduction is RIP, a death domain–containing protein kinase that participates in both activation of NFκB and promotion of apoptosis (*10*). Whereas FADD is required for TNF-R1–induced apoptosis, the interaction of TRADD with TRAF2 is required for activation of NFκB and is dispensable for cytotoxicity (*5, 9*).

In addition to inducing apoptosis and activation of NFκB, cross-linking of TNF-R1 activates SAPK, also known as c-Jun NH_2-terminal kinase (JNK). SAPK binds to and phosphorylates the transcription factor c-Jun within its NH_2-terminal domain in cells exposed to environmental stresses [including TNF, ultraviolet (UV) light, protein synthesis inhibitors, and thermal stress] (*11*). The physiological consequences of SAPK activation have not been thoroughly defined. However, it has been shown that SAPK activity is required for apoptosis in nerve growth factor–deprived sympathetic neurons (*12*), as well as for stress-induced apoptosis in both leukemia cells and fibroblasts (*13*).

We therefore investigated the molecular mechanisms and the significance of TNF-induced activation of SAPK. Human embryonic kidney 293 cells contain very small amounts of endogenous TNF-R2, whereas TNF-R1 is constitutively expressed. Therefore, in these cells soluble TNF induces only TNF-R1 signaling (*5, 9*). Treatment of 293 cells with human recombinant TNF-α (hrTNF-α) induces a rapid and transient in-

G. Natoli, A. Costanzo, A. Ianni, M. Levrero, Fondazione Andrea Cesalpino and Istituto di I Clinica Medica, Policlinico Umberto I, Viale del Policlinico 155, 00161 Rome, Italy.
D. J. Templeton, Case Western Reserve University School of Medicine, Biomedical Research Building, Cleveland, OH 44106, USA.
J. R. Woodgett, Ontario Cancer Institute–Princess Margaret Hospital, Toronto M5G 2M9, Canada.
C. Balsano, Dipartimento di Medicina Interna, Università di L'Aquila, L'Aquila, 67100, Italy.

*To whom correspondence should be addressed.